Revision 2

Carbonate mineralization in percolated olivine aggregates: Linking effects of crystallographic orientation and fluid flow

Steve Peuble [1,*], Muriel Andreani [2], Marguerite Godard [1], Philippe Gouze [1], Fabrice Barou [1], Bertrand Van de Moortele [2], David Mainprice [1], Bruno Reynard [2]

[1]Géosciences Montpellier, Université Montpellier 2, CNRS, Place Eugène Bataillon cc060, F-34095 Montpellier Cedex 5, France

[2]Laboratoire de Géologie de Lyon: Terre, Planètes, Environnement, ENS-Université Lyon 1, CNRS, F-69622 Villeurbanne, France

* Corresponding author. Tel.: + 33 467143944.
E-mail address: Steve.Peuble@gm.univ-montp2.fr

1. Abstract

In situ mineralization of CO_2 in ultramafic rock-hosted aquifers is one of the promising solutions for decreasing CO_2 concentrations in the atmosphere. Naturally altered ultramafic rocks suggest that carbonation processes are controlled by local heterogeneities in the structure of the rock and fluid transport at the water-rock interfaces. We studied the role of rock crystallographic anisotropy relative to the global fluid flow direction on the mineralization of CO_2 by means of electron microscope analyses from the macro- to the micrometer scale (EBSD-FIB). The sample used for the measurements was a hot pressed olivine core percolated by water enriched in CO_2 (pCO_2=10 MPa) at 180°C. During the percolation experiment, olivine was dissolved and two types of carbonates, dolomite and magnesite, were precipitated on olivine surfaces. The results showed that the dissolution of olivine is controlled by its crystallographic properties as shown by the development of etch-pits only on the $(010)_{ol}$ *planes* and with elongated shapes parallel to the $[010]_{ol}$ *axes*. In

Always consult and cite the final, published document. See http://www.minsocam.org or GeoscienceWorld

contrast, the precipitation of carbonates is governed by hydrodynamic properties. Carbonates are heterogeneously distributed in the percolated rock. They are mainly located along the moderate (for dolomite) and the minor (for magnesite) flow paths, both oriented parallel to the principal fluid flow direction, which allow carbonates to be supplied with divalent cations (e.g. Ca^{2+}, Mg^{2+} and Fe^{2+}). In these flow paths, carbonate growth is systematically oriented normal to the flow that facilitates the development of chemical gradients with cationic supersaturation conditions for carbonate precipitation near the walls.

In natural systems, the $(010)_{ol}$ *planes* are parallel to the Moho and the $(100)_{ol}$ *planes* are vertical; our study suggests that flow of CO_2-rich fluids will induce precipitation of carbonates localized along, and preferentially clogging, vertical flow paths while favoring olivine dissolution along horizontal fluid pathways. This dual control of structure and fluid flow on carbonation mechanisms could be an important parameter allowing sustainable CO_2 storage in peridotites while limiting the risks of leakage toward the surface.

Keywords:

EBSD-FIB, CO_2 mineralization, ultramafic rocks, etch-pits, oriented growth, crystallographic relationships.

2. Introduction

In situ carbonation of ultramafic rocks is potentially an effective and safe means for mitigating atmospheric carbon dioxide (CO_2) concentrations (Bachu et al., 1994; Goff and Lackner, 1998; Jun et al., 2013; Matter and Kelemen, 2009; Oelkers et al., 2008; Seifritz, 1990). Carbonation (or CO_2 mineralization) consists in transforming CO_2 into stable

Always consult and cite the final, published document. See http://www.minsocam.org or GeoscienceWorld

carbonates through a suite of chemical fluid-rock reactions; it is a process commonly observed in natural ophiolitic (for example, Kelemen and Matter, 2008; Kelemen et al., 2011) and oceanic environments (for example, Alt and Teagle, 1999; Bach et al., 2004; Kelley et al., 2005; Ludwig et al., 2006). These chemical reactions are coupled to the transport of reactants and products of reactions at the fluid-mineral interface: first, CO_2 reacts with water to produce H^+ and bicarbonates/carbonates ions (HCO_3^-/CO_3^{2-}); the H^+ ions then trigger the dissolution of silicate minerals and bicarbonates/carbonates ions combine with the divalent cations provided by silicate dissolution and/or fluids precipitate carbonates (Kelemen et al., 2011). Ultramafic rocks are widely distributed at the Earth's surface (Bodinier and Godard, 2003; Deschamps et al., 2013); they also have the highest potential to mineralize CO_2 due to their high proportion of divalent cations (40-50 weight % MgO ± CaO ± FeO) and their high reactivity (Matter and Kelemen, 2009; Oelkers et al., 2008; Xu et al., 2004). Thus they could represent one of the natural sinks for atmospheric CO_2 (Alt and Teagle, 1999; Früh-Green et al., 2004). They are also a possible target for industrial CO_2 geological storage (Kelemen and Matter, 2008; Matter and Kelemen, 2009), provided the development of methods allowing to overcome the mechanisms limiting carbonation kinetics (e.g., formation of silica layer on dissolving olivine grains (Johnson et al., 2014; Sissmann et al., 2013)); this requires a better understanding of the mechanisms driving carbonation reactions in ultramafic systems..

Laboratory experiments and natural observations of altered peridotites indicate that carbonation reactions are controlled by fluid flow and also by the structure of the reacting rocks (e.g. Andreani et al., 2009; Kelemen and Matter, 2008). Kelemen and Matter (2008) reported a geometric distribution of carbonate veins in altered ophiolite outcrops (Samail ophiolite, Sultanate of Oman). The veins show a possible organization of the carbonation processes (i.e. dissolution of olivine and precipitation of carbonates) with respect to the fluid

Always consult and cite the final, published document. See http://www.minsocam.org or GeoscienceWorld

circulation in the altered peridotites and/or the initial structure of the rock (e.g. pores/fractures geometry, fracture network, rock anisotropy, crystallographic orientation). Serpentinization, another natural example of olivine alteration could also be controlled by the coupling between fluid flow and rock structure. Boudier et al. (2009) showed a control of mantle peridotite anisotropy, inherited from the asthenospheric mantle flow, on water flow during serpentinization at mid-ocean ridges. They proposed that the topography of olivine-serpentine interfaces was governed by the $(100)_{olivine}$ *microcracks* forming vertical and open fluid pathways in the cooling lithospheric mantle. Laboratory percolation experiments conducted on porous olivine-rich aggregates also point to the strong effect of pore geometry and thus of the local heterogeneities in fluid flow on the nature and efficiency of hydration and CO_2 mineralization processes (Andreani et al., 2009; Godard et al., 2013; Peuble et al., 2014). Finally, etch-pits formed during the dissolution of olivine are generally limited to certain surfaces suggesting a control by the crystallographic properties of olivine (e.g. Arvidson and Luttge, 2010; Daval et al., 2013; Dove et al., 2005; Grandstaff, 1978; King et al., 2010; King et al., 2014; Lasaga and Blum, 1986; Velbel and Ranck, 2008). Awad et al. (2000) showed that the dissolution rate of olivine is the highest along its $[010]_{ol}$ *axes* (~10 times higher than the other *axes*) due to the olivine dense atomic packing in this plane.

Although natural and experimental observations indicate a possible control of fluid flow and of the rock structure on the mineralization of CO_2, the respective roles of these parameters are still poorly understood. In this paper we investigate the interplay between fluid flow distribution and the rock structure, in particular we focus on the role of mineral crystallographic orientation and pore-fracture network, in olivine aggregates, to improve the modeling of the sustainability of carbonation in ultramafic aquifers. We performed Electron Backscatter Diffraction (EBSD) analyses at millimeter to micrometer scale on two initially

Always consult and cite the final, published document. See http://www.minsocam.org or GeoscienceWorld

similar olivine cores (ø 6.35 mm × L 13 mm), one of them having been percolated by a CO_2-rich fluid at P-T conditions analogous to that expected for *in situ* carbon storage (Peuble et al., 2014).

3. Material & method

Analyses have been performed on two mineral aggregates composed of olivine Fo_{87}. The first olivine-rich aggregate (sample H0; ϕ = 5.71 %) is the control sample. The second sample (sample H2; ϕ = 6.02 %) was percolated during 56 hrs by a CO_2-rich fluid at controlled temperature and pressure conditions (T=185°C; p_{CO2} = 10 MPa; P_{total} = 12 MPa) at a constant flow injection rate of 0.1 $mL.h^{-1}$. The injected fluid was a 0.57M $NaHCO_3$ solution prepared with MilliQ water and "pure grade" Panreac salts; it contained trace amounts of Ca and Si brought in by the Panreac salts. The conditions, methodology and results of the experiment are summarized in Appendix 1 and detailed in a companion paper (Peuble et al., 2014).

Both sintered porous aggregates were obtained by first, compacting the olivine powder using uniaxial cold-pressing (T = 25°C; P_{axial} = 5 MPa), then sintering the compacted aggregate by isotropic hot-pressing (T = 1180°C; $P_{confining}$ = 150 MPa) using a gas-medium high-pressure and high-temperature vessel (Paterson, 1990).

After the percolation experiment, the reacted core samples were cut in half along the cylinder axis (i.e. parallel to the main fluid flow direction) and polished for EBSD analyses. The sample was dry sawed and impregnated in an Araldite® 2020 epoxy. Pre-polishing was then made with sandpapers (from 120 to 2400 FEPA standards). Final polishing was performed with diamond paste from 6 to 0.25 µm. Lubrication was performed with Vaseline® oil to avoid carbonate dissolution. The sample was cleaned at each step of polishing with dishwashing liquid, rinsed with alcohol and finally dried with compressed air.

Always consult and cite the final, published document. See http://www.minsocam.org or GeoscienceWorld

Directions and dips of fracture planes in the control and percolated olivine-rich aggregates were measured using an optical microscope equipped with a five axes U-stages (Geosciences Montpellier, France). Measurements were realized with the X *axis* parallel to the cylinder axis.

Backscattered (BSE) and secondary electron (SE) images were obtained using FEI Quanta FEG 200 Scanning Electron Microscope installed at the University of Montpellier 2 (France). This device operated at an acceleration voltage of 15 kV and a water partial pressure about 93.3 Pa.

Crystal structures of the control and the percolated aggregates were determined by EBSD analyses performed at the sample scale and at the micrometer scale. Sample scale EBSD analyses were made with a CamScan X500FE CrystalProbe equipped with an EBSD system (Geosciences Montpellier, France). Charging effects on the uncoated rock were avoided by low vacuum conditions with a chamber pressure of 5 Pa and an acceleration voltage of 15 kV. For each scanning point, interactions of electrons with sample surface produced a diffraction pattern fitted with a set of 8 Kikuchi lines to deduce the nature and orientation of the crystal. Results were recorded on digital CCD camera. Indexation was made with a step of 4 μm between each point of measurement. In order to increase forward scattered electron (FSE) yield, the sample surface is inclined at 20° respectively to the electron beam for sample scale EBSD analyses. This provides the best compromise between sufficient electron diffraction pattern intensity and good spatial resolution. But the hardness of olivine is different from that of carbonates: it is therefore not possible to avoid steps between those two phases even with very careful polishing. Because of the sample inclination any topographic defect is amplified and this can lead to shadowing at the olivine-carbonates interfaces. To further characterize the interface, micrometer scale EBSD analyses were performed on 150 nm thick TEM lamella

Always consult and cite the final, published document. See http://www.minsocam.org or GeoscienceWorld

prepared by Focused Ion Beam (ZEISS NVision 40 Focused Ion Beam). Two TEM lamellae were made in the inlet zone of the percolated sample. The sample was previously coated with a 20 nm-thick carbon layer. A 10-15 nm-thick layer of carbon was deposited by induced electron beam to avoid amorphization of the sub-surface (i.e. 10-20 nm). A thicker layer of carbon was added by FIB induced deposition (1-2 µm) to protect TEM lamellae during the observations. Excavations were made on the top and bottom of the TEM lamella at each location. All millings were performed with a 30 kV ion beam. TEM lamella was separated from the bulk sample and lifted out when a depth between 1 and 2 µm was reached. It was fixed by carbon ion-beam deposition on a classical half copper grid. The TEM lamella thickness was reduced to the desired value of 150 nm with an olivine-carbonates interface free of topography and then cleaned for traces of Ga ion implantation at 2 kV-50 pA during 1 min. Transmission-EBSD (Keller and Geiss, 2012), also called transmission Kikuchi diffraction (Trimby, 2012); was performed on the TEM lamellae with a ZEISS Supra 55 VP equipped with a Nordlys Sensitive camera (Oxford Instruments). TEM lamellae were tilted about 20° respectively to the electron beam (Keller and Geiss, 2012; Trimby, 2012). The measurement step size was 50 and 80 nm for the first and the second TEM lamellae, respectively. Carbonates have been indexed using the structural x-ray cell, where the perfect cleavage rhombohedral *plane* (r) has the indices (10-14).

After the EBSD acquisition on both scales, data have been processed with the CHANNEL-5 software (Oxford Instruments HKL) to delete all the grains with a diameter of less than 3 times the measurement step size and thus remove the measurement uncertainties. Then, Euler angle triplets (α, β, γ), corresponding to the orientation of each crystal in the rock, are described by using radially symmetric kernel functions and orientation distribution function (ODF). Data are first approximated by a linear combination of the individual unimodal bell-shaped kernels (Hielscher and Schaeben, 2008) and then treated using the MatLab open-

Always consult and cite the final, published document. See http://www.minsocam.org or GeoscienceWorld

source and free toolbox MTEX (Bachmann et al., 2010; Hielscher and Schaeben, 2008) (http://code.google.com/p/mtex/). The default kernel for texture analysis in MTEX is the De la Vallée-Poussin kernel, which has the unique property that it is exactly represented in spherical harmonics (Schaeben, 1999) with a 10° half-width. The resulting crystal preferred orientation (CPO) of each mineral phase was plotted as pole figures. Accuracy of statistical analyses was ensured by a large number of grains obtained during measurements. Sample scale data were reduced to one point per grain analyses to study the precipitation processes of minerals present in very small volume fractions. All grains measured on the FIB sections are represented on the pole figures because this representation allows the characterization of any crystallographic orientation changes within carbonates at a micrometer scale.

4. Results

4.1 Unreacted olivine-rich aggregate

The EBSD measurements of the orientation distribution of the olivine aggregate before the percolation experiment are presented first. The $[100]_{ol}$ and $[010]_{ol}$ *axes* are respectively oriented perpendicular and parallel to the X *direction* corresponding to the cylindrical axis of the core sample (see Figure 1). The $[001]_{ol}$ *axes* are more dispersed throughout the pole figure. Optical measurements reveal the formation of a large fracture networks within the olivine grains resulting from the uniaxial cold-pressing of the ultramafic powder. These fractures, on average 10 µm wide, are generally straight and parallel to each other. The poles to these fracture planes are correlated with the $[100]_{ol}$ *axes* indicating that fractures are parallel to the $(100)_{ol}$ *planes* (Figure 1).

4.2 Percolated olivine-rich aggregate

Always consult and cite the final, published document. See http://www.minsocam.org or GeoscienceWorld

4.2.1 Sample scale analyses

The percolation of the CO_2-rich water into sample H2 resulted in the dissolution of olivine initially present in the aggregate and the precipitation of secondary phases: carbonates (dolomite, magnesite) upstream and serpentine-type minerals downstream. When referring to crystallographic directions and planes we will use the subscripts ol, carb, mgn, dol for olivine, carbonates, magnesite and dolomite respectively. Olivine has the same CPO as the control sample (see Figure 2): the $[100]_{ol}$ and $[010]_{ol}$ *axes* are dominantly oriented normal and parallel to the X *axis*, respectively, while the $[001]_{ol}$ *axes* are more scattered in the pole figure with a slight concentration parallel to the Z *axis*. The main fluid flow direction was therefore oriented parallel to the dominant alignment of $(100)_{ol}$ and $(001)_{ol}$ *planes*, and normal to the $(010)_{ol}$ *planes* during the percolation experiment. Optical measurements revealed the same arrangement of the fracture network as previously observed on the control sample (Figure 1). Indexed points on the EBSD map allowed the identification of dolomite and magnesite representing 1.41 % and 0.61 % of the total sample surface, respectively. These carbonates have a strong CPO in the percolated sample with the $r[10\text{-}14]_{carb}$ and $c[0001]_{carb}$ *axes* both oriented normal to the cylinder axis (i.e. the X *axis*). The $a(2\text{-}1\text{-}10)_{dol}$ *planes* of dolomite and the $m(10\text{-}10)_{mgn}$ *planes* of magnesite are both aligned in the cylinder axis. In both carbonates, the $c[0001]_{carb}$ *axis*, which is the unique axis without multiplicity in carbonates crystals, is the most concentrated axis with a maximum of 24 and 19 times a uniform distribution for dolomite and magnesite, respectively (Figure 2). Carbonates are also highly correlated with olivine crystal orientations in two preferred models: $[100]_{ol}$ *axes* || $c[0001]_{dol}$ *axes* ; $(010)_{ol}$ *planes* || $a(2\text{-}1\text{-}10)_{dol}$ *planes* for dolomite and $[001]_{ol}$ *axes* || $c[0001]_{mgn}$ *axes* ; $(010)_{ol}$ *planes* || $m(10\text{-}10)_{mgn}$ *planes* for magnesite, where || signifies parallel.

Always consult and cite the final, published document. See http://www.minsocam.org or GeoscienceWorld

4.2.2 Micrometer scale characterization

Dissolution areas

The dissolution of olivine is marked by symmetrical and regular etch-pits preferentially limited to the olivine surfaces oriented normal to the main fluid flow direction (Figures 3a and b). We recognized two types of dissolution figures. The first consists of small polyhedral mounts with amplitudes less than 1 μm and oriented perpendicular to the olivine surface (Figure 3a). The second forms conical shaped peaks (up to 5 μm) limited to the $(010)_{ol}$ *planes* and with elongation normal to the surface, hence parallel to $[010]_{ol}$ *axes* (Figure 3b).

Precipitation areas

Carbonates are heterogeneously distributed in the percolated rock at the sample scale (Peuble et al., 2014) and at the pore scale (see Figures 3c and 4). They are observed only within the first 5 mm at the fluid inlet and, depending on their composition, they are distributed in specific areas. Dolomite precipitates in fractures formed in olivine during uniaxial cold-pressing (Fig. 3c) and magnesite is observed mainly on former dissolution sites at olivine grain boundaries (Fig. 4). Chemical maps indicate that the precipitation of magnesite is locally accompanied by microparticles of silica and calcite in the adjacent narrow pores (Figure 4). The calcite grains were too few and too small to be identified by EBSD analyses.

The crystallographic contact between olivine and carbonates was studied by the FIB-EBSD method. Two FIB sections were cut perpendicular to the olivine fracture planes (in which dolomite precipitated), oriented normal and parallel to the cylinder axis respectively (see Figure 5). On the first FIB section (Figure 5a-d), the five olivine grains have the same CPO but it is different from that previously described at the sample scale: the $[100]_{ol}$ *axes* are grouped in the XY *plane* while the $[010]_{ol}$ and $[001]_{ol}$ *axes* are both oriented oblique to the X

Always consult and cite the final, published document. See http://www.minsocam.org or GeoscienceWorld

axis (i.e. the cylinder axis). In contrast, dolomite grains have the same CPO as that of the sample scale: the r[10-14]$_{dol}$ and c[0001]$_{dol}$ *axes* are both oriented subparallel to the Y *axis* and normal to the X *axis*. The a(2-1-10)$_{dol}$ *planes* are subparallel to the cylinder axis.

On the second FIB section (Figure 5e-h), the olivine CPO is also different from that observed at the sample scale: the [100]$_{ol}$ and [010]$_{ol}$ *axes* are both oriented oblique to the X *axis* and the [001]$_{ol}$ *ones* are parallel to the *Z axis*. But again, dolomite grains have the strong CPO as in the rest of the sample: the r[10-14]$_{dol}$ and c[0001]$_{dol}$ *axes* are still oriented perpendicular to the cylinder axis (i.e. the X *axis*) while the a(2-1-10)$_{dol}$ *planes* are aligned with the cylinder axis.

5. Discussion

5.1 What factors control olivine dissolution?

The control and percolated olivine-rich aggregates have the same anisotropic structure marked by the (010)$_{ol}$ *planes* perpendicular to the cylindrical *axis* of the core sample (Figure 6). This anisotropy was acquired during the sample preparation when the uniaxial cold-pressing of the olivine-rich powder oriented [010]$_{ol}$ *axes* parallel to the main compression (σ_1), mimicking the natural behavior of mantle peridotites submitted to pure shear (Jung et al., 2006; Mainprice et al., 2000; Tommasi et al., 1999). Uniaxial cold-pressing (T = 25°C; P_{axial} = 5 MPa) moreover promoted the propagation of a dense fracture networks along the (100)$_{ol}$ *planes* also observed in natural samples; the (100)$_{ol}$ *plane* being the preferential plane for edge dislocation in olivine (Boudier et al., 2009; Gaboriaud et al., 1981; Nicolas and Poirier, 1976). During the percolation experiment, the (100)$_{ol}$ *fracture planes* were oriented subparallel to the main fluid flow direction; it is worth noting that in peridotite outcrops, similarly oriented fracture networks have been proposed as major flow paths during the serpentinization of mantle peridotites (Boudier et al., 2009). These observations lead to the

Always consult and cite the final, published document. See http://www.minsocam.org or GeoscienceWorld

following question: could the initial heterogeneities in the rock structure govern the dissolution of olivine during CO_2-rich fluid injection in ultramafic aquifers?

In the percolated sample, the dissolution of olivine results in the development of symmetrical etch-pits limited to the $(010)_{ol}$ *surfaces* and with an elongation axis parallel to the $[010]_{ol}$ *axes*. Similar figures have been described in the literature on experimental (Awad et al., 2000; Grandstaff, 1978; King et al., 2010; King et al., 2014; Malvoisin et al., 2012; Wegner and Christie, 1976) and natural samples (Velbel, 2009; Velbel and Ranck, 2008). They are generally restricted to some olivine surfaces suggesting that the dissolution of this mineral is anisotropic (King et al., 2010; King et al., 2014).

In our study, etch-pits indicate a preferential dissolution of olivine along the $(010)_{ol}$ *surfaces*, which can be explained by three reasons. First, the $(010)_{ol}$ *plane* is the preferred cleavage plane in the olivine crystal (Atkinson and Meredith, 1987; Boudier et al., 2009). Cleavage could lead to the formation of microdefects along the $(010)_{ol}$ *plane*, which could then facilitate the anisotropic dissolution of olivine (associated with the development of etch-pits) as noted in several studies (Arvidson and Luttge, 2010; Daval et al., 2013; Dove et al., 2005; Lasaga and Blum, 1986).

Second, the $(010)_{ol}$ *plane* has also been described as the plane with the greatest reactive surface area in the olivine crystal due to its largest faces inter-planar spacing (Donnay and Harker, 1937). This could facilitate fluid-rock interactions (and thus dissolution) along this plane, especially since it is oriented normal to the main fluid flow direction. Because of this orientation, much of the fluid has been in contact with the $(010)_{ol}$ *planes* during the injection. The fluid that is not yet enriched in Mg, Fe, Si (i.e. the products of olivine dissolution) remains in an undersaturated state, which drives the dissolution of olivine and the etch-pits growth (Godinho et al., 2012 and references therein; Lüttge, 2005; Smith et al., 2013). Etch-

Always consult and cite the final, published document. See http://www.minsocam.org or GeoscienceWorld

pits may then change the mineral topography (Lüttge, 2005), reinforcing the anisotropic dissolution of olivine by increasing the reactive surface areas of the $(010)_{ol}$ *planes*.

Third, the anisotropic dissolution of olivine could be produced by its crystallography. Previous studies proposed a stronger chemical affinities of H^+ with atoms present along the $(010)_{ol}$ *planes* because these planes have the highest negative net charge in the olivine crystal due to more abundant $O_{(1)}$ type oxygen (Awad et al., 2000 and references therein).

5.2 On the control of fluid flow on carbonation

The main products of olivine dissolution (i.e. Fe, Mg and Si) were mixed and transported along different flow paths in the percolated rock. Optical and SEM observations coupled with EBSD analyses have identified four types of flow paths in the olivine-rich aggregate: (i) the main flow paths are formed by the larger pores of the sample (up to 50 μm) interconnected to each other independently of the olivine crystallography, (ii) secondary flow paths formed along the 10 μm wide $(100)_{ol}$ *fracture planes* oriented parallel to the main fluid flow direction, (iii) minor flow paths located at the olivine grain boundaries along the $(001)_{ol}$ *planes*, i.e. narrower paths than the $(100)_{ol}$ *fractures* but still oriented parallel to the main fluid flow direction, and finally, (iv) those with a more restricted flow along the olivine grain boundaries oriented perpendicular to the flow i.e. the $(010)_{ol}$ *surfaces*. Carbonates were essentially localized along the secondary and the minor flow rate paths of the percolated sample. They show a strong crystallographic relationship with olivine, marked by: $[100]_{ol}$ *axes* || $c[0001]_{dol}$ *axes* and $[001]_{ol}$ *axes* || $c[0001]_{mgn}$ *axes* (Figure 6). But no strong crystallographic correlation was observed on both FIB sections, which suggests a non-topotactic growth of carbonates on the olivine surfaces.

Always consult and cite the final, published document. See http://www.minsocam.org or GeoscienceWorld

315 However, at all scales, the r$[10\text{-}14]_{carb}$ *axis*, marking the preferential carbonate growth
316 direction (Churakov et al., 2004; Jordan et al., 2001; Pokrovsky and Schott, 2002; Schott et
317 al., 2009), is systematically oriented normal to the main fluid flow direction. EBSD-FIB
318 analyses also indicate that there is no change in the crystallographic orientation of carbonates
319 during their growth as the $(10\text{-}14)_{dol}$ *pole figures* show only one maximum for each FIB
320 section (see Figures 5d and 5h). These results suggest that the precipitation of carbonates is
321 controlled by the fluid flow rate in relation to the initial structure of the aggregate. Carbonates
322 nucleated preferentially on olivine surfaces oriented parallel to the flow (i.e. along the
323 secondary and minor flow paths of the rock) and then grew with a systematic orientation
324 normal to the flow. The secondary and minor flow paths of the olivine aggregate are wide
325 enough to provide abundant cation arrival and small enough to reduce locally the flow rate,
326 maintaining local supersaturation conditions for carbonate precipitation. This interpretation is
327 consistent with Andreani et al. (2009) showing the preferential distribution of carbonates in
328 reduced-flow zones. Similarly, a slight chemical gradient develops perpendicular to the main
329 fluid flow direction and the nucleation of carbonates is preferentially located where the fluid
330 velocity field tends toward zero, i.e. on the $(100)_{ol}$ and $(001)_{ol}$ *surfaces*. This arrangement
331 facilitates the growth of carbonates sustaining a large interaction area between the $(10\text{-}14)_{carb}$
332 *planes* and the fluid. This plane is also known to control the kinetics of carbonate
333 precipitation by promoting the adsorption of hydrated species ($>CO_3Me^{+}\cdot nH_2O$; with Me
334 representing a divalent metal cation like Ca^{2+}, Mg^{2+}, Fe^{2+}) at the surface of carbonates
335 (Pokrovsky and Schott, 2002; Saldi et al., 2009; Schott et al., 2009).

336 Our results indicate changes in the distribution of carbonates within the rock depending on
337 fluid pathways: dolomite was typically localized in secondary flow paths while magnesite
338 preferentially formed in minor fluid pathways. This suggests that variations in pores/fractures

Always consult and cite the final, published document. See http://www.minsocam.org or GeoscienceWorld

339 geometry (i.e. size, distribution, connectivity and orientation) impact the local fluid flow
340 (local changes in velocity, …) and thus the solution composition which, in turn, impacts
341 mineral reactivity and carbonate precipitation. The $(100)_{ol}$ *fracture planes* favor (i) the supply
342 of products from different sources mixed together in the fluid flow (magnesium and iron from
343 the olivine dissolution; calcium from the fluid) and (ii) nucleation points on numerous defects
344 induced by fracturing, both of which promote the precipitation of dolomite. The formation of
345 magnesite is limited to more confined flow zones. The precipitation of magnesite is
346 kinetically less favored than that of Ca-rich carbonates because of the different chemical
347 properties of Mg^{2+} and Ca^{2+} ions (Pokrovsky and Schott, 2002; Schott et al., 2009): the
348 limiting step for carbonate crystallization is the divalent metal cation dehydration at the
349 surface i.e. the formation of surface metal sites ($>MeOH_2^+$) from hydrated adsorbed species
350 ($>CO_3Me^+ \cdot nH_2O$) (Pokrovsky and Schott, 2002 and references therein). The rate of water
351 molecule exchange from the fluid into the cation hydration sphere is faster for Ca^{2+} than Mg^{2+}
352 (Casey and Westrich, 1992; Pokrovsky and Schott, 2002) and this mechanism provides a way
353 to explain the difference in the precipitation rates of Ca-rich (fast) and Mg-rich (slow)
354 carbonates . This may explain that : (i) both dolomite and magnesite are observed in the
355 percolated olivine-rich aggregate although the fluid/rock system is rich in magnesium and
356 poor in calcium, and (ii) magnesite is limited to the narrow olivine grain boundaries, where
357 fluid renewal (and thus the supply in Ca^{2+}) is less efficient (e.g. minor flow paths). However,
358 when the chemical conditions are favorable for its precipitation, magnesite will thrive
359 (growing up to ten microns in thickness) regardless of other chemical products (e.g. Si, Ca)
360 precipitating as isolated microparticles in the surrounding narrow pores.

361 **6. Implications for *in situ* mineralization of CO_2**
362

Always consult and cite the final, published document. See http://www.minsocam.org or GeoscienceWorld

Olivine dissolution and carbonate precipitation are two independent processes, controlled by different chemical conditions, yet intimately coupled. The dissolution of olivine is promoted by H^+ while the precipitation of carbonates is induced by cationic supersaturation conditions mainly provided by olivine dissolution. Thus, *in situ* mineralization of CO_2 in the ultramafic aquifer may persist in the long term only if specific chemical conditions are satisfied. This study suggests that these chemical conditions are locally facilitated by the structural anisotropy characterizing the host rock: the orthorhombic fabric of olivine is oriented (such that $(100)_{ol}$ *planes* are statistically vertical and $(010)_{ol}$ *planes* horizontal) and the fractures network is preferentially developed along the $(100)_{ol}$ *planes* sub-boundary (or dislocation wall). Mantle peridotites typically display a structural anisotropy characterized by the crystallographic preferred orientations of silicate minerals that have a much stronger CPOs than in our cold pressed samples. Serpentinised oceanic lithosphere has $(010)_{ol}$ *planes* aligned in the asthenospheric mantle flow direction and the preferred fracture planes which represent the preferential flow paths for hydrothermal fluids are $(100)_{ol}$ (Boudier et al., 2009; Mainprice et al., 2000; Nicolas and Poirier, 1976). The circulation of the fluid in the percolated aggregate was controlled by the vertical flow paths created along the $(100)_{ol}$ *fracture planes* is similar to what has been observed in serpentinised oceanic mantle lithosphere.

Because mantle peridotites have a $(100)_{ol}$ *fracturing* and an orthorhombic olivine fabric inherited from the asthenospheric mantle flow, carbonates are expected to have a preferred direction for precipitation in natural ultramafic aquifers, inherited from the host rock structure and its hydrodynamic properties. This allows the extrapolation of our results to larger scale models to simulate *in situ* mineralization of CO_2 in natural ultramafic reservoirs. In this case, we expect that olivine will be preferentially dissolved along $(010)_{ol}$ *surfaces*, assuming horizontal fabrics similar to what has been observed by Boudier et al. (2009). The CPO of

Always consult and cite the final, published document. See http://www.minsocam.org or GeoscienceWorld

mantle peridotites found in ophiolite massifs targeted for CO_2 sequestration (e.g. Oman) are dominated by an olivine CPO with the a-*axis* and c-*axis* horizontal and b-*axis* vertical, this CPO represents over 70% of the Ben Ismaïl and Mainprice (1998) CPO database. The resulting dissolution products will be easily transported through various flow paths in the percolated rock, including the $(100)_{ol}$ *fracture planes* oriented parallel to the main direction of fluid percolation for a vertical injection well. During percolation into the ultramafic aquifer, H^+ are progressively consumed onto the $(010)_{ol}$ *dissolution surfaces* to form silica and water (e.g., Matter et al., 2011), which are then converted into silicic acid carried away in the fluid. This will cause a local increase in the fluid pH. The concentration of divalent cations will also increase which will facilitate the nucleation and growth of carbonates. Precipitation will be favored perpendicular to the main fluid flow direction (i.e. vertical fluid flow), on the $(100)_{ol}$ *fracture planes* and the $(001)_{ol}$ *surfaces*, both aligned parallel to the flow. The composition of carbonates will depend on local fluid flow conditions: Ca-rich carbonates will precipitate in moderate flow paths when water contains Ca even in a Mg-rich reservoir, and magnesite will precipitate in zones of more reduced flow conditions (rock dominated systems). This implies that a good knowledge of the reservoir structure could allow predicting the preferential areas of silicate dissolution and of precipitation of various carbonates in the host rock. It suggests also that the rate of *in situ* mineralization of CO_2 can be enhanced (i) in presence of calcium (provided by the fluid and/or the dissolution of Ca-rich silicates) and (ii) by decreasing the flow injection rate to facilitate the precipitation of Mg-rich carbonates. But these results also indicate that the precipitation of carbonates is located along vertical flow paths in the reservoir, with a risk of clogging the pore network of the host rock. This could in turn favor horizontal fluid flow within the aquifer along the $(010)_{ol}$ *dissolution planes*.

Always consult and cite the final, published document. See http://www.minsocam.org or GeoscienceWorld

The sustainability of CO_2 storage in highly reactive systems such as ultramafic reservoirs will mainly depend on an efficient dissolution of olivine to provide divalent cations for carbonate precipitation. The dual control of the structure of ultramafic rocks and fluid flow on carbonation processes could also be an important parameter favoring sustainable carbon storage by maintaining horizontal flow paths and thus allowing continuous CO_2 injection into the ultramafic reservoir over long periods while limiting the risks of leakages toward the surface.

7. Acknowledgments

This research was supported by the ANR (CO2FIX-ANR-08-PCO2-003-02), CNRS (PIE-HY-GEO) and Université Montpellier 2 (Programme-Pluridisciplinaire-Energie). We also thank C. Nevado and D. Delmas for the preparation of the polished sections. CLYM (FED 4092) was acknowledged for FIB ZEISS NVision40 access. We thank MATEIS lab. at INSA de Lyon for the use of the ZEISS SUPRA 55 VP. We thank Damien Daval, Bill Bassett and an anonymous reviewer for their detailed comments and suggestions and Haozhe Liu for editorial handing.

Figure captions

Figure 1: Analyses of the olivine-rich aggregate before the percolation experiment. (a) Sketch of the sintered olivine core (ø 6.35 mm × L 13 mm) on which was realized the polished section parallel to the X *axis* (cylinder axis and main flow direction during percolation experiments). (b) Pole figures showing the crystal preferred orientation (CPO) of the olivine grains (n = 4 479). Lower hemisphere projection; one point per grain. The minimum and maximum densities are respectively written on the left and right sides of each pole figures. The Electron Back Scattered Diffraction (EBSD) data were previously smoothed using the

Always consult and cite the final, published document. See http://www.minsocam.org or GeoscienceWorld

kernel De la Vallee-Poussin function with a 10° full-width-at-half-maximum (FWHM). See text and methods section for more details. (c) On the left side, plot of poles to fracture planes. Data are presented as equal area on lower-hemisphere projection. On the right side, fractures formed parallel to the X *axis* within the olivine grains (optical microscope, transmitted light).

Figure 2: EBSD analyses performed on the percolated olivine-rich aggregate at the sample scale. The polished section was realized along the main fluid flow direction (X *axis*). Band contrast EBSD map (a) and pole figures (b) of the three minerals present in the reacted sample such as olivine (n = 15 423), dolomite (n = 226) and magnesite (n = 100). The units of map axes are in µm. Pole figure data are projected on lower hemisphere with one point per grain representation. Pole figures are represented with [hkl] *axes* and (uvw) *planes* Miller indices for olivine and carbonates, respectively. The minimum and maximum densities of EBSD data are written on the left and right sides, respectively, of each pole figure. Note that sample polishing created a shift in relief between olivine and carbonates. Consequently, dolomites for which the $r[10\text{-}14]_{carb}$ and $c[0001]_{carb}$ *axes* are strictly horizontal are not quantified on the EBSD analyses because they are hidden by fractures wherein they precipitated.

Figure 3: Scanning electron microscope images showing dissolution figures (a, b) and carbonate precipitation areas (c) in the percolated sample. (a) Polyhedral and micrometer mounts developed on specific olivine (Ol.) surfaces oriented normal to the main fluid flow direction. (b) Conical shaped peaks observed on the $(010)_{ol}$ *plane* with elongation axes parallel to the $[010]_{ol}$ *axis*. (c) Dolomite (Dol.) precipitation in the olivine fractures.

Figure 4: Chemical maps showing the repartition of all compiled cations (a), Si (b), Ca (c) and Mg (d) in a sample pore located in the extremity at which the fluid entered the rock. The cation concentrations are highlighted by the point densities measured on each chemical map. Results show large magnesite grain localized at the olivine grain boundaries. Black ellipses

Always consult and cite the final, published document. See http://www.minsocam.org or GeoscienceWorld

458 present on image (a) symbolize the surrounding olivine grain boundaries containing Ca-rich
459 micrograins and Si amorphous material.

460 **Figure 5**: EBSD analyses performed on the percolated olivine-rich aggregate at a micrometer
461 scale using FIB (Focused Ion Beam) sections. The first FIB section (a, b, c) was realized
462 parallel to the X *axis* (i.e. the main fluid flow direction) and the second one (e, f, g)
463 perpendicular to the X *axis*. Images (a) and (e) show the areas where both FIB sections were
464 cut (white squares). The axes of olivine fracture planes are symbolized by white dotted lines.
465 (b) and (f) illustrate both thinned FIB sections attached on the sample holder. (c) and (g) show
466 the EBSD maps of olivine (light gray) and dolomite (dark gray) grains on both FIB sections.
467 (d) and (h) are the corresponding pole figures results. Pole figures data are projected on lower
468 hemisphere with all measured points representation.

469 **Figure 6**: Schematic model deduced from the results of this study. The sample preparation
470 oriented the $[010]_{ol}$ *axis* parallel to the main fluid flow direction and promoted an intense
471 fracturing along the $(100)_{ol}$ *planes*. These rock heterogeneities facilitated the precipitation of
472 dolomite along the $(100)_{ol}$ *fractures* acting as secondary flow paths during fluid injection and
473 of magnesite on the $(001)_{ol}$ *surfaces* where olivine grain boundaries ensured more reduced-
474 flow conditions. Olivine dissolution is crystallographically controlled by the atoms present on
475 its $(010)_{ol}$ *planes* leading to the development of etch-pits on $(010)_{ol}$ *surfaces* and with
476 elongation axes parallel to $[010]_{ol}$ *axes*.

477

478 **References**

479 Alt, J.C., and Teagle, D.A.H. (1999) The uptake of carbon during alteration of ocean crust.
480 Geochimica et Cosmochimica Acta, 63(10), 1527-1535.

Always consult and cite the final, published document. See http://www.minsocam.org or GeoscienceWorld

Andreani, M., Luquot, L., Gouze, P., Godard, M., Hoise, E., and Gibert, B. (2009) Experimental study of carbon sequestration reactions controlled by the percolation of CO_2-rich brine through peridotites. Environmental Science & Technology, 43(4), 1226-1231.

Arvidson, R.S., and Luttge, A. (2010) Mineral dissolution kinetics as a function of distance from equilibrium–New experimental results. Chemical Geology, 269(1), 79-88.

Atkinson, B.K., and Meredith, P.G. (1987) Experimental fracture mechanics data for rocks and minerals. Fracture mechanics of rock, 477-525.

Awad, A., Koster Van Groos, A.F., and Guggenheim, S. (2000) Forsteritic olivine: effect of crystallographic direction on dissolution kinetics. Geochimica et Cosmochimica Acta, 64(10), 1765-1772.

Bach, W., Garrido, C.J., Harvey, J., Paulick, H., and Rosner, M. (2004) Variable seawater–peridotite interactions —first insights from ODP Leg 209, MAR 15°N. Geochemistry Geophysics Geosystems, 5(9), Q09F26.

Bachmann, F., Hielscher, R., and Schaeben, H. (2010) Texture Analysis with MTEX - Free and Open Source Software Toolbox. Solid State Phenomena, 160, 63-68.

Bachu, S., Gunter, W.D., and Perkins, E.H. (1994) Aquifer disposal of CO_2: hydrodynamic and mineral trapping. Energy Conversion Management, 35, 269-279.

Ben Ismaı□l, W., and Mainprice, D. (1998) An olivine fabric database: an overview of upper mantle fabrics and seismic anisotropy. Tectonophysics, 296(1), 145-157.

Bodinier, J.-L., and Godard, M. (2003) Orogenic, ophiolitic, and abyssal peridotites. Treatise on geochemistry, 2, 103-170.

Boudier, F., Baronnet, A., and Mainprice, D. (2009) Serpentine mineral replacements of natural olivine and their seismic implications: oceanic lizardite versus subduction-related antigorite. Journal of Petrology, 51(1-2), 495-512.

Always consult and cite the final, published document. See http://www.minsocam.org or GeoscienceWorld

505 Casey, W.H., and Westrich, H.R. (1992) Control of dissolution rates of orthosilicate minerals
506 by divalent metal–oxygen bonds. Nature, 355(6356), 157-159.
507 Churakov, S.V., Iannuzzi, M., and Parrinello, M. (2004) Ab Initio study of dehydroxylation-
508 carbonation reaction on brucite surface. Journal of Physical Chemistry, 108, 11567-11574.
509 Daval, D., Hellmann, R., Saldi, G.D., Wirth, R., and Knauss, K.G. (2013) Linking nm-scale
510 measurements of the anisotropy of silicate surface reactivity to macroscopic dissolution rate
511 laws: New insights based on diopside. Geochimica et Cosmochimica Acta, 107, 121-134.
512 Deschamps, F., Godard, M., Guillot, S., and Hattori, K. (2013) Geochemistry of subduction
513 zone serpentinites: A review. Lithos.
514 Donnay, J.D.H., and Harker, D. (1937) A new law of crystal morphology extending the law of
515 Bravais. American Mineralogist, 22(5), 446-467.
516 Dove, P.M., Han, N., and De Yoreo, J.J. (2005) Mechanisms of classical crystal growth
517 theory explain quartz and silicate dissolution behavior. Proceedings of the National Academy
518 of Sciences of the United States of America, 102(43), 15357-15362.
519 Früh-Green, G.L., Connolly, J., Plas, A., Kelley, D.S., and Grobety, B. (2004)
520 Serpentinization of oceanic peridotites: implications for geochemical cycles and biological
521 activity. Geophysical monograph series, 144, 119-136.
522 Gaboriaud, R.J., Darot, M., Gueguen, Y., and Woirgard, J. (1981) Dislocations in olivine
523 indented at low temperatures. Physics and Chemistry of Minerals, 7, 100-104.
524 Godard, M., Luquot, L., Andreani, M., and Gouze, P. (2013) Incipient hydration of mantle
525 lithosphere at ridges: a reactive-percolation experiment. Earth and Planetary Science Letters,
526 371, 92-102.
527 Godinho, J.R.A., Piazolo, S., and Evins, L.Z. (2012) Effect of surface orientation on
528 dissolution rates and topography of CaF_2. Geochimica et Cosmochimica Acta, 86, 392-403.

Always consult and cite the final, published document. See http://www.minsocam.org or GeoscienceWorld

529 Goff, F., and Lackner, K.S. (1998) Carbon dioxide sequestering using ultramafic rocks.
530 Environmental Geosciences, 5(3), 89-101.
531 Grandstaff, D.E. (1978) Changes in surface area and morphology and the mechanism of a
532 forsterite dissolution. Geochimica et Cosmochimica Acta, 42, 1899-1901.
533 Hielscher, R., and Schaeben, H. (2008) A novel pole figure inversion method: specification of
534 the MTEX algorithm. Journal of Applied Crystallography, 41, 1024-1037.
535 Johnson, N.C., Thomas, B., Maher, K., Rosenbauer, R.J., Bird, D., and Brown Jr, G.E. (2014)
536 Olivine dissolution and carbonation under conditions relevant for in situ carbon storage.
537 Chemical Geology, 373, 93-105.
538 Jordan, G., Higgins, S.R., Eggleston, C.M., Knauss, K.G., and Schmahl, W.W. (2001)
539 Dissolution kinetics of magnesite in acidic aqueous solution, a hydrothermal atomic force
540 microscopy (HAFM) study: Step orientation and kink dynamics. Geochimica et
541 Cosmochimica Acta, 65(23), 4257-4266.
542 Jun, Y.-S., Giammar, D.E., and Werth, C.J. (2013) Impacts of geochemical reactions on
543 geologic carbon sequestration. Environmental Science & Technology, 47(1), 3-8.
544 Jung, H., Katayama, I., Jiang, Z., Hiraga, T., and Karato, S. (2006) Effect of water and stress
545 on the lattice-preferred orientation of olivine. Tectonophysics, 421, 1-22.
546 Kelemen, P.B., and Matter, J. (2008) In situ carbonation of peridotite for CO_2 storage.
547 Proceedings of the National Academy of Sciences, 105(45), 17295–17300.
548 Kelemen, P.B., Matter, J., Streit, E.E., Rudge, J.F., Curry, W.B., and Blusztajn, J. (2011)
549 Rates and mechanisms of mineral carbonation in peridotite: natural processes and recipes for
550 enhanced, in situ CO_2 capture and storage. Annual Review of Earth and Planetary Sciences,
551 39, 546-576.
552 Keller, R.R., and Geiss, R.H. (2012) Transmission EBSD from 10 nm domains in a scanning
553 electron microscope. Journal of Microscopy, 245(3), 245-251.

Always consult and cite the final, published document. See http://www.minsocam.org or GeoscienceWorld

554 Kelley, D.S., Karson, J.A., Früh-Green, G.L., Yoerger, D.R., Shank, T.M., Butterfield, D.A.,
555 Hayes, J.M., Schrenk, M.O., Olson, E.J., and Proskurowski, G. (2005) A serpentinite-hosted
556 ecosystem: the Lost City hydrothermal field. Science, 307(5714), 1428-1434.
557 King, H.E., Plumper, O., and Putnis, A. (2010) Effect of secondary phase formation on the
558 carbonation of olivine. Environmental Science & Technology, 44, 6503-6509.
559 King, H.E., Satoh, H., Tsukamoto, K., and Putnis, A. (2014) Surface-specific measurements
560 of olivine dissolution by phase-shift interferometry. American Mineralogist, 99(2-3), 377-
561 386.
562 Lasaga, A.C., and Blum, A.E. (1986) Surface chemistry, etch pits and mineral-water
563 reactions. Geochimica et Cosmochimica Acta, 50(10), 2363-2379.
564 Ludwig, K.A., Kelley, D.S., Butterfield, D.A., Nelson, B.K., and Früh-Green, G.L. (2006)
565 Formation and evolution of carbonate chimneys at the Lost City Hydrothermal Field.
566 Geochimica et Cosmochimica Acta, 70(14), 3625-3645.
567 Lüttge, A. (2005) Etch pit coalescence, surface area, and overall mineral dissolution rates.
568 American Mineralogist, 90(11-12), 1776-1783.
569 Mainprice, D., Barruol, G., and Ben Ismail, W. (2000) The seismic anisotropy of the Earth's
570 mantle : from single crystal to polycrystal, in Earth's deep interior : Mineral Physics and
571 Tomography from the atomic to the global scale. In S. Karato, Forte, A.M., Liebermann,
572 R.C., Masters, G., Stixrude, L., Ed. Mineral Physics and Seismic Tomography: From Atomic
573 to Global, 117, p. 237-264. AGU Geophysical Monograph 117.
574 Malvoisin, B., Brunet, F., Carlut, J., Rouméjon, S., and Cannat, M. (2012) Serpentinization of
575 oceanic peridotites: 2. Kinetics and processes of San Carlos olivine hydrothermal alteration.
576 Journal of Geophysical Research, 117.
577 Matter, J., Broecker, W.S., Gislason, S.R., Gunnlaugsson, E., Oelkers, E.H., Stute, M.,
578 Sigurdardottir, H., Stefansson, A., Alfredsson, H.A., Aradottir, E.S., Axelsson, B., Sigfusson,

Always consult and cite the final, published document. See http://www.minsocam.org or GeoscienceWorld

B., and Wolff-Boenisch, D. (2011) The CarbFix Pilot Project - Storing Carbon Dioxide in Basalt. Energy Procedia, 4(5579-5585).

Matter, J.M., and Kelemen, P.B. (2009) Permanent storage of carbon dioxide in geological reservoirs by mineral carbonation. Nature Geoscience, 2, 837-841.

Nicolas, A., and Poirier, J.P. (1976) Crystalline plasticity and solid state flow in metamorphic rocks. John Wiley, London.

Oelkers, E.H., Gislason, S.R., and Matter, J. (2008) Mineral carbonation of CO_2. Elements, 4, 333-337.

Paterson, M.S. (1990) Rock deformation experimentation. Geophysical monograph series, 56, 187-194.

Peuble, S., Godard, M., Luquot, L., Andreani, M., Martinez, I., and Gouze, P. (2014) CO_2 geological storage in olivine rich basaltic aquifers: New Insights from flow-through experiments. Applied Geochemistry.

Pokrovsky, O.S., and Schott, J. (2002) Surface chemistry and dissolution kinetics of divalent metal carbonates. Environmental Science & Technology, 36(3), 426-432.

Saldi, G.D., Jordan, G., Schott, J., and Oelkers, E.H. (2009) Magnesite growth rates as a function of temperature and saturation state. Geochimica et Cosmochimica Acta, 73, 5646-5657.

Schaeben, H. (1999) The De La Vallée-Poussin standard orientation density function. Textures and Microstructures, 33, 365-373.

Schott, J., Pokrovsky, O.S., and Oelkers, E.H. (2009) The link between mineral dissolution/precipitation kinetics and solution chemistry. Reviews in Mineralogy & Geochemistry, 70, 207-258.

Seifritz, W. (1990) CO_2 disposal by means of silicates. Nature, 345, 486.

Always consult and cite the final, published document. See http://www.minsocam.org or GeoscienceWorld

Sissmann, O., Daval, D., Brunet, F., Guyot, F., Verlaguet, A., Pinquier, Y., Findling, N., and Martinez, I. (2013) The deleterious effect of secondary phases on olivine carbonation yield: Insight from time-resolved aqueous-fluid sampling and FIB-TEM characterization. Chemical Geology, 357, 186-202.

Smith, M.E., Knauss, K.G., and Higgins, S.R. (2013) Effects of crystal orientation on the dissolution of calcite by chemical and microscopic analysis. Chemical Geology, 360, 10-21.

Tommasi, A., Tikoff, B., and Vauchez, A. (1999) Upper mantle tectonics: three-dimensional deformation, olivine crystallographic fabrics and seismic properties. Earth and Planetary Science Letters, 168, 173-186.

Trimby, P.W. (2012) Orientation mapping of nanostructured materials using transmission Kikuchi diffraction in the scanning electron microscope. Ultramicroscopy, 120, 16-24.

Velbel, M.A. (2009) Dissolution of olivine during natural weathering. Geochimica et Cosmochimica Acta, 73(20), 6098-6113.

Velbel, M.A., and Ranck, J.M. (2008) Etch pits on naturally altered olivine from dunites of the Appalachian Blue Ridge Mountains, North Carolina, USA. Mineralogical Magazine, 72(1), 145-148.

Wegner, M.W., and Christie, J.M. (1976) Chemical etching of dislocations in forsterite. Contributions to Mineralogy and Petrology, 59, 131-140.

Xu, T., Apps, J.A., and Pruess, K. (2004) Numerical simulation of CO_2 disposal by mineral trapping in deep aquifers. Applied Geochemistry, 19, 917-936.

Always consult and cite the final, published document. See http://www.minsocam.org or GeoscienceWorld

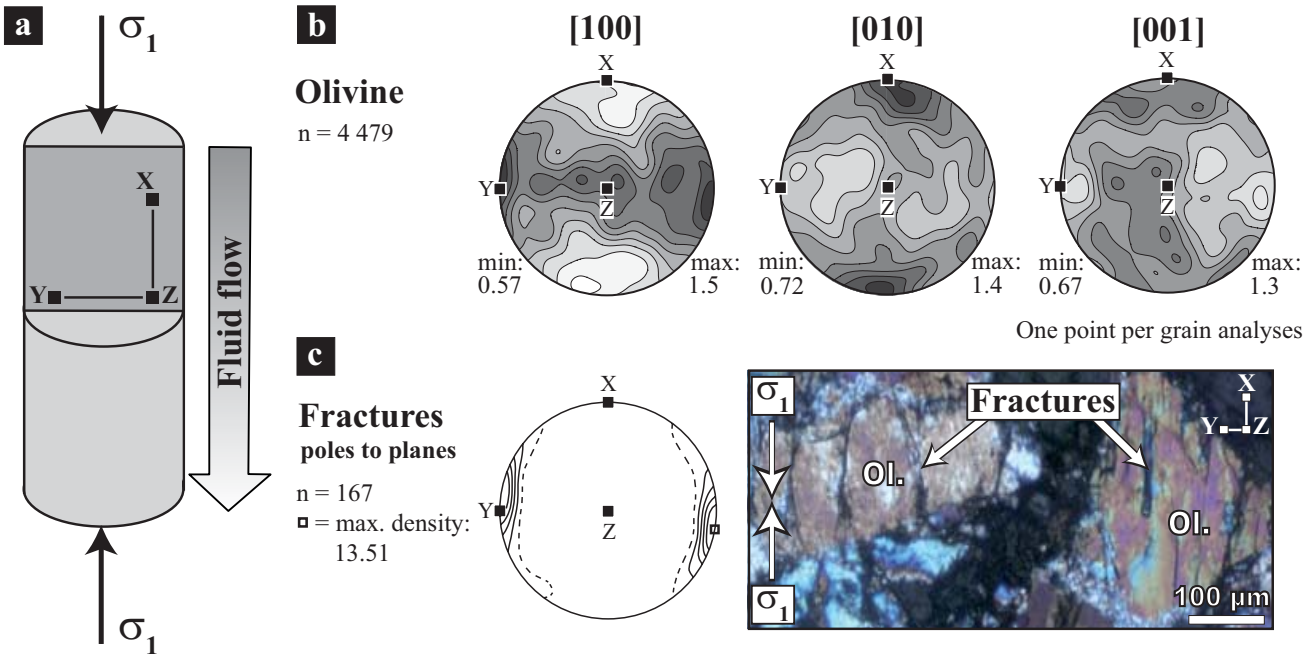

Figure 1. Am.Min. Peuble et al. 2014

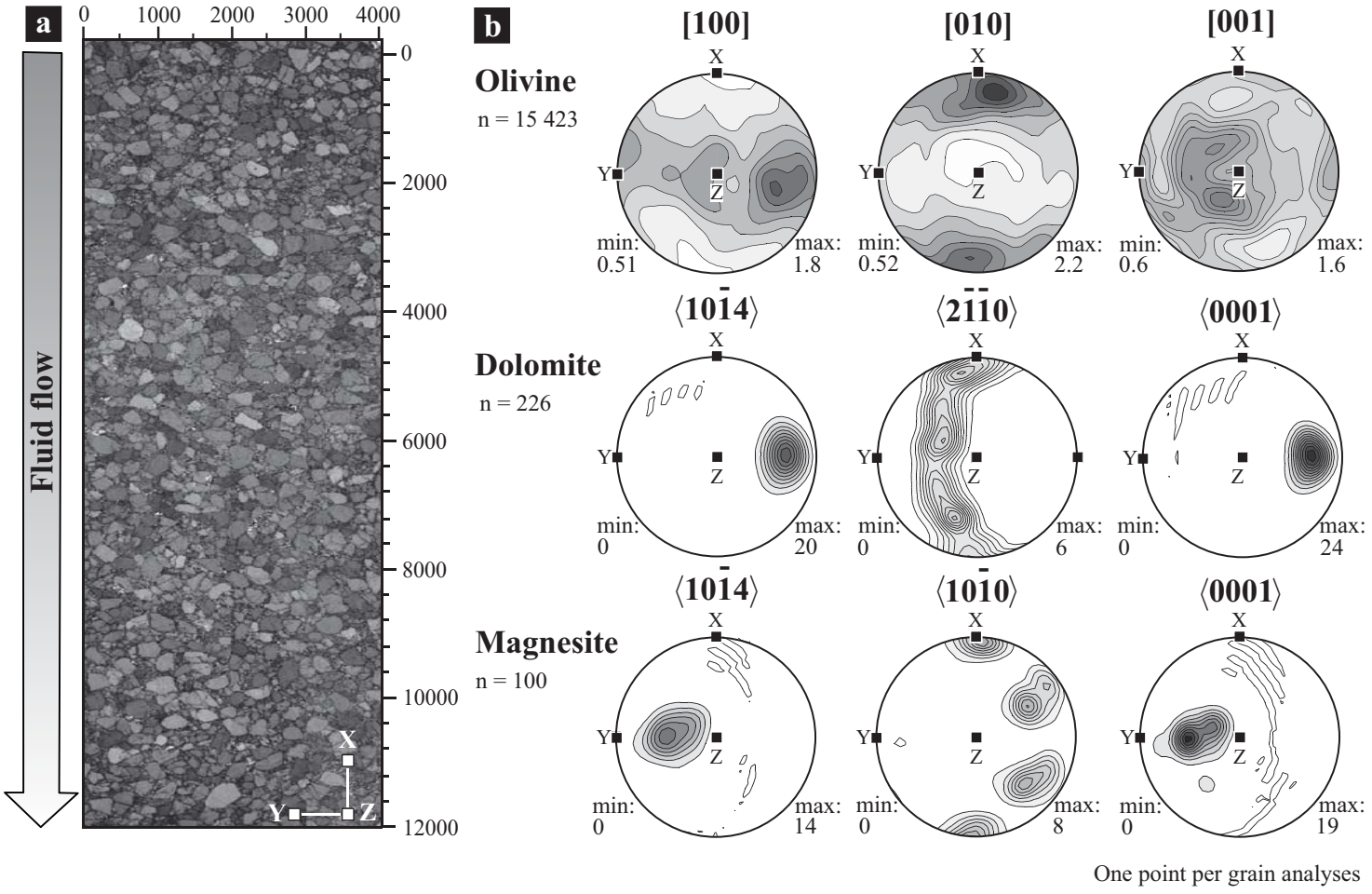

Figure 2. Am.Min. Peuble et al. 2014

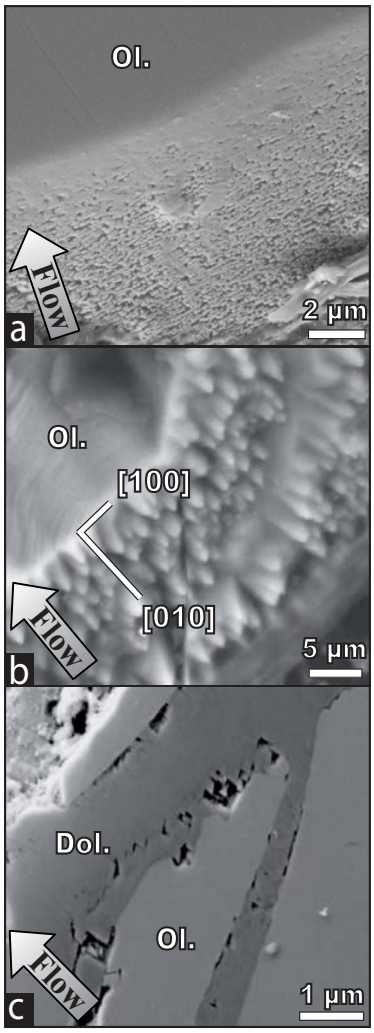

Figure 3. Am.Min. Peuble et al. 2014

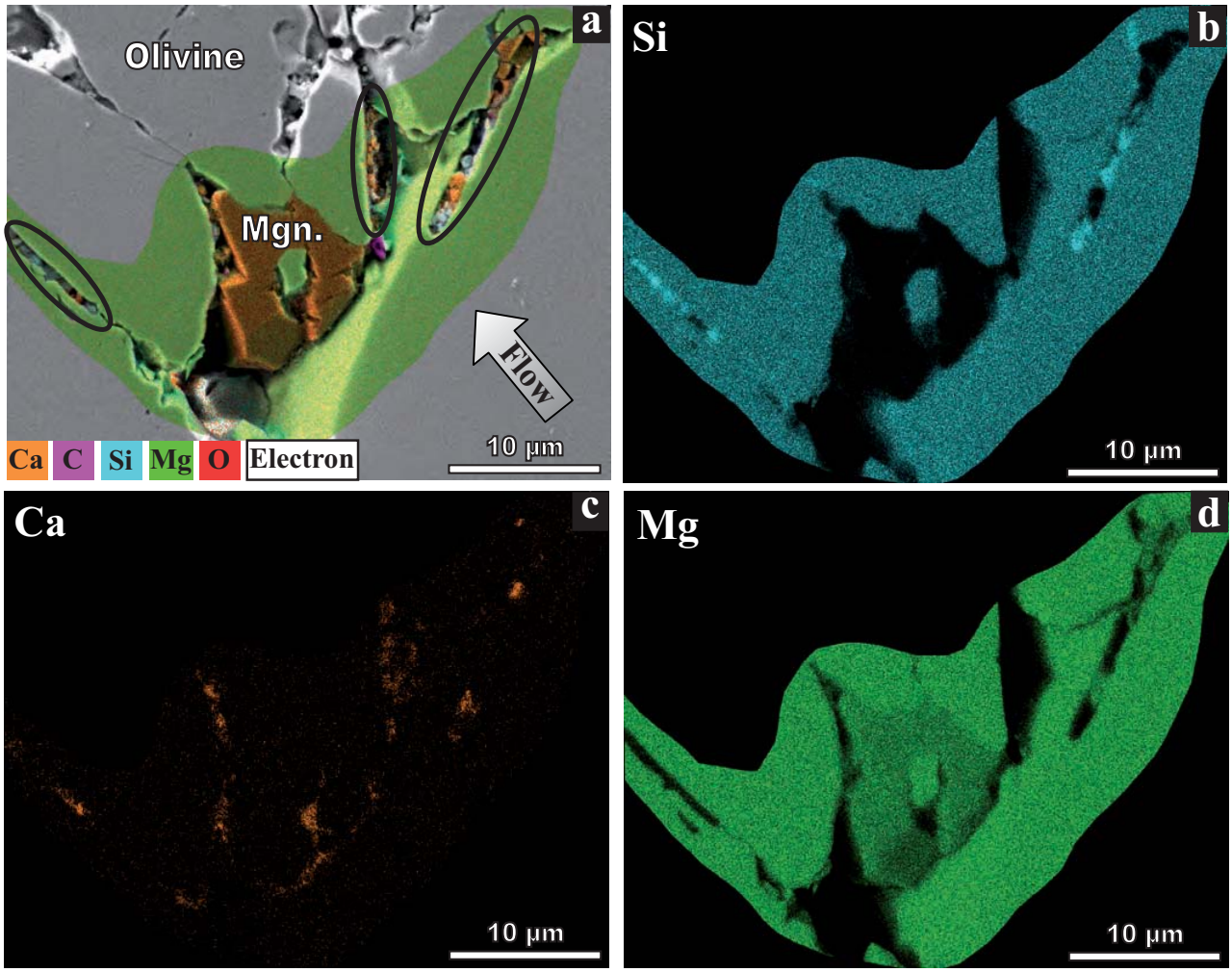

Figure 4. Am.Min. Peuble et al. 2014

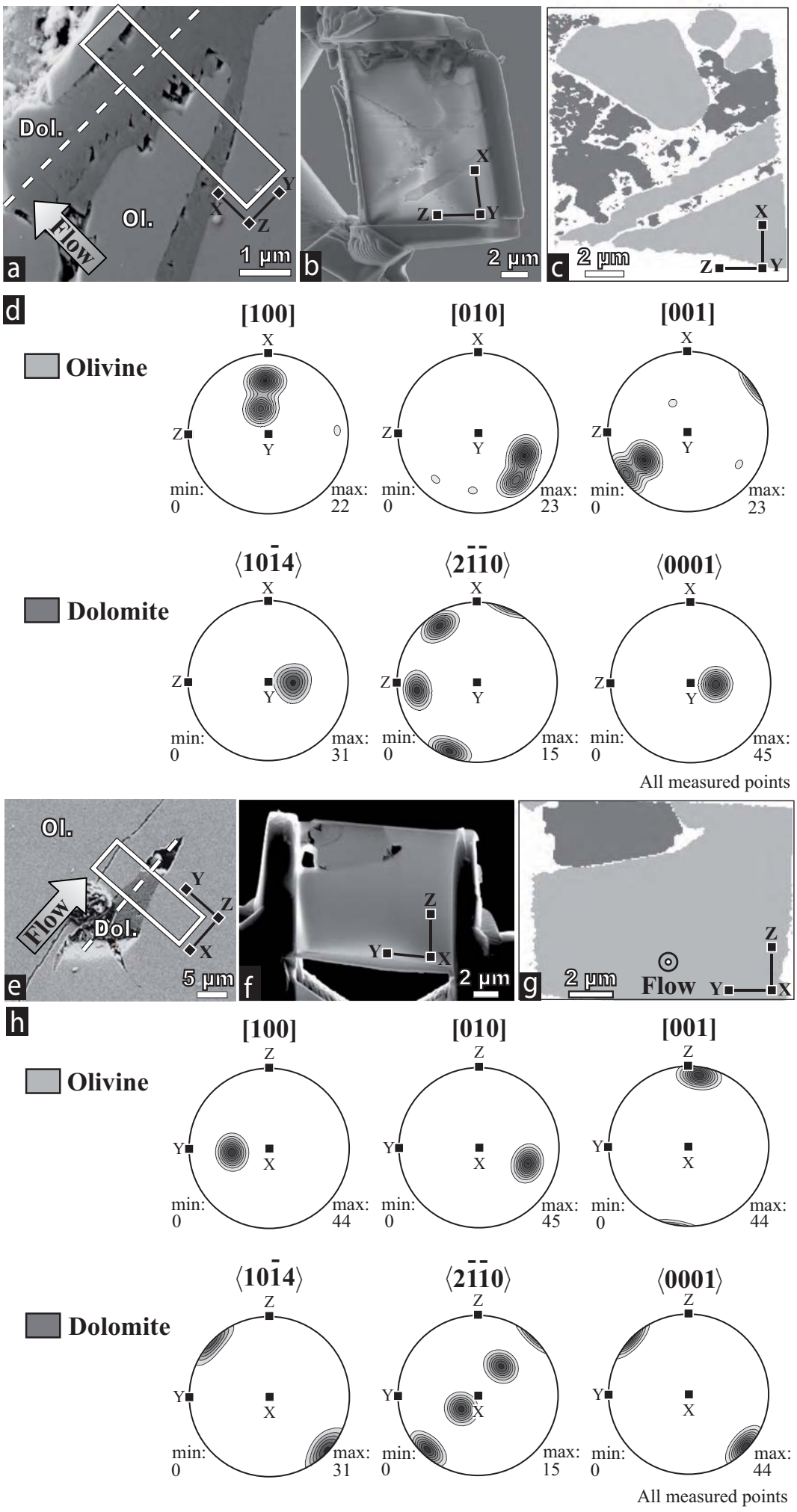

Figure 5. Am.Min. Peuble et al. 2014

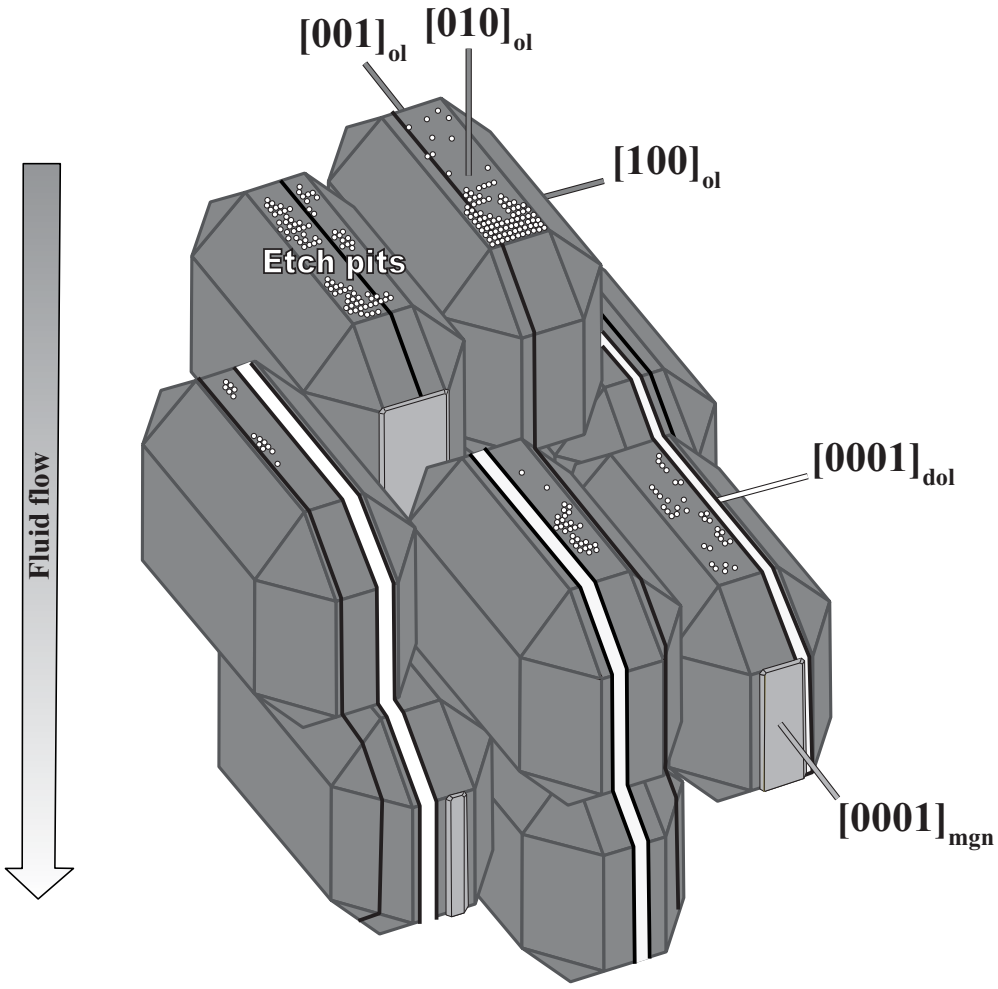

Figure 6. Am.Min. Peuble et al. 2014